

Organic-inorganic hybrid molecules for elastic ceramic plastic with covalent-ionic bicontinuous network

Zhaoming Liu (✉ oldliu@zju.edu.cn)

Zhejiang University <https://orcid.org/0000-0002-7564-6207>

Weifeng Fang

Zhejiang University

Zhao Mu

Zhejiang University

Yan He

Zhejiang University

Kangren Kong

<https://orcid.org/0000-0002-0395-2280>

Kai Jiang

East China Normal University

Ruikang Tang

Zhejiang University <https://orcid.org/0000-0001-5277-7338>

Physical Sciences - Article

Keywords:

Posted Date: October 7th, 2022

DOI: <https://doi.org/10.21203/rs.3.rs-2112637/v1>

License:   This work is licensed under a Creative Commons Attribution 4.0 International License.

[Read Full License](#)

Version of Record: A version of this preprint was published at Nature on June 7th, 2023. See the published version at <https://doi.org/10.1038/s41586-023-06117-1>.

Abstract

Transformations of molecules to bulk materials constitute a unique direction for rational design of materials, known as bottom-up syntheses. Although organic-inorganic hybrid materials have played indispensable roles as mechanical, optical, electronic, and biomedical materials, isolated organic-inorganic hybrid molecules (currently only limited in covalent compounds) seldom presented throughout the preparation of hybrid materials, which is due to the distinct behaviours of organic covalent bonds and inorganic ionic bonds in molecular construction. Here, we integrate typical covalent and ionic bonds within one molecule to create an organic-inorganic hybrid molecule, which can be used for bottom-up syntheses of hybrid materials. A combination of the organic covalent thioctic acid (TA) and the inorganic ionic calcium carbonate oligomer (CCO) via an acid-base reaction provided a TA-CCO hybrid molecule, and its representative molecular formula was $\text{TA}_2\text{Ca}(\text{CaCO}_3)_2$. Its dual reactivity involving copolymerization of the organic TA-segment and inorganic CCO-segment generated the respective covalent and ionic networks. The two networks were interconnected and integrated by each TA-CCO complex to form a covalent-ionic bicontinuous structure within the resulting hybrid material, poly(TA-CCO), which synchronously achieved unification of paradoxical mechanical properties, i.e., hardness versus resilience and strength versus deformability. Moreover, the dynamic $\text{Ca}^{2+}\text{-CO}_3^{2-}$ bonds in the ionic network and S-S bonds in the covalent network ensured material recyclability with plastic-like mouldability while preserving thermal stability. The coexistence of ceramic-like, rubber-like and plastic-like behaviours within poly(TA-CCO) goes beyond current classifications of materials, following the generation of the “elastic ceramic plastic”. The demonstrated bottom-up creation of organic-inorganic hybrid molecules, covalent-ionic bicontinuous networks and ultimately unique materials provides a feasible pathway for design and construction of hybrid materials by molecular engineering, thereby supplementing the classical methodology used for manufacture of organic-inorganic hybrid materials.

Full Text

The lack of organic-inorganic covalent-ionic molecules (a molecule containing both organic covalent compounds and inorganic ionic compounds as molecular segments) prohibits the production of diverse organic-inorganic hybrid materials in a “bottom-up” way¹⁶. The traditional inorganic preparation by nucleation commonly skips the molecular stages of inorganic ionic substances¹⁷⁻¹⁹, which creates a knowledge gap regarding inorganic ionic molecules and their reactions with organic covalent molecules. It prevents the fusion of organic and inorganic ionic substances from molecule to bulk material, both in structure and performance^{20,21}. However, our recent finding on “inorganic ionic oligomer” creates the possibility for preparation of molecule-sized inorganic ionic substances²², which opens a window for creation of organic-inorganic covalent-ionic molecules and the subsequent “bottom-up” preparation of hybrid materials. Here, we chose CCO (with the molecular formula $(\text{CaCO}_3)_3$), which can crosslink to bulk materials²², and thioctic acid (TA), which can polymerize through dynamic disulfide bonds²³ (S-S), as examples of inorganic and organic molecules, respectively. We

achieved hybridization of CCO and TA molecules by using a general acid-base reaction in classical chemistry.

Typically, hybridization was achieved by adding CCO (Extended Data Fig. 1a, b) dropwise into an ethanol solution of TA (Extended Data Fig. 1c). The carboxyl groups of TA gradually bonded to the Ca^{2+} of CCO through a subsequent acid-base reaction (Fig. 1a), and a solution of the TA-CCO hybrid molecule was prepared. The resulting TA-CCO hybrid molecules were detected by electrospray ionization mass spectrometry (ESI-MS) (Fig. 1b): the major negatively charged peaks appeared at 171, 205, and 305 m/z after subtracting the background. The peaks at $m/z = 171$ and 205 were attributed to the characteristic fragment ions of TA (Extended Data Fig. 1d), and the main peak at $m/z = 305$ referred to a structure of $(\text{TA-CaCO}_3)_2^{2-}$, which directs to a molecular formula of $\text{TA}_2\text{Ca}(\text{CaCO}_3)_2$ before ionization. By using inductively coupled plasma–optical emission spectrometry (ICP–OES), we confirmed that the average molar ratio of Ca to TA was $\approx 1.5:1$, which is in good agreement with the proposed molecular formula for TA-CCO hybrid molecules (Extended Data Fig. 2a). The liquid-state nuclear magnetic resonance (NMR) spectroscopy demonstrated typical shifts of 159.82, 181.18 and 57.03 ppm, which corresponded to carbonate, carboxyl group, and tertiary carbon in the carbon ring of TA, respectively (Fig. 1c, Extended Data Fig. 2b, c). This further confirmed the presence of CaCO_3 and TA molecular segments in the TA-CCO hybrid molecule, $\text{TA}_2\text{Ca}(\text{CaCO}_3)_2$. The symmetry of the peaks for carbonate (160 ppm) and carboxyl group (181 ppm) suggested similar chemical environments for carbonate and TA, respectively, implying a symmetrical molecular structure for $\text{TA}_2\text{Ca}(\text{CaCO}_3)_2$ (Fig. 1a, Extended Data Fig. 2d). In contrast, CaCO_3 nanoparticles and TA did not form hybrid molecules but organic–inorganic nanocomposites, which is consistent with common understanding (Extended Data Fig. 2e-h).

The interactions of organic and inorganic ionic segments in the TA-CCO hybrid molecule were analysed by Fourier transform infrared (FTIR) and X-ray photoelectron spectroscopy (XPS). The FTIR spectrum showed an absorption peak for the in-plane bending vibration (ν_3) of CO_3^{2-} at 1399 cm^{-1} in amorphous CaCO_3 , while it was blueshifted to 1414 cm^{-1} for TA-CCO. Meanwhile, the C=O stretching vibration of the carboxyl group in TA appeared at 1691 cm^{-1} , and it was redshifted to 1559 cm^{-1} in TA-CCO (Fig. 1d). The shifts in the FTIR spectra indicated formation of ionic bonds between the carboxyl group in TA and the carbonate of CaCO_3 . XPS confirmed the shift of the Ca 2p peak from 346.90 eV in CaCO_3 to 347.25 eV in TA-CCO (Fig. 1e). These results indicated a change in the orbital electron density of calcium, which was caused by the higher binding energy between Ca^{2+} and carboxyl groups. These indicated the construction of covalent-ionic electrostatic interactions in TA-CCO hybrid molecules.

High-resolution transmission electron microscopy (HRTEM) showed TA-CCO hybrid molecules with an average size of 3.2 nm (Fig. 1f, Extended Data Fig. 3a), which fit the simulated size of $(\text{TA}_2\text{Ca}(\text{CaCO}_3)_2)$ (Extended Data Fig. 3b). The inorganic ionic segments of TA-CCO hybrid molecules enable its inorganic crosslinking, which was demonstrated by *in situ* X-ray diffraction (XRD). We calculated the total pair distribution (TDF) via integration of the peak at approximately 2.4 \AA , which is a typical peak for the first

coordination shell of Ca-O^{24} . The increase in the TDF integration indicated crosslinking of TA-CCO by inorganic ionic bonds formed under mild conditions²² (Fig. 1g). Meanwhile, the dynamic disulfide bonds from the organic segment underwent a ring-opening reaction during thermal treatment^{25,26} (Fig. 1h, Extended Data Fig. 3c), which led to polymerization of the TA-CCO. Therefore, the TA-CCO hybrid molecules could realize crosslinking and polymerization synchronously under reasonable conditions (Fig. 1i).

Hot pressing (120 °C, 110 MPa) was used in this work to start the crosslinking and polymerization processes of the TA-CCO hybrid molecule in a condensed state, which led to a transparent yellow poly(TA-CCO) bulk (Fig. 2a right). A suitable mould ensured the formation of the poly(TA-CCO) bulk into different shapes (triangles, squares, rectangles, etc.), as seen when making thermoplastics²⁷ (Extended Data Fig. 4a inset). Typically, the yellow colour resulted from absorption by TA segment in TA-CCO (Extended Data Fig. 4a, b). The cross-sectional image generated by focused ion beam scanning electron microscopy (FIB-SEM) showed a continuous structure for the poly(TA-CCO) bulk from the macroscale to the microscale (Fig. 2b). Energy-dispersive X-ray spectroscopy (EDS) indicated that the elements Ca, S, O, and C were uniformly dispersed in the poly(TA-CCO) bulk (Fig. 2c). This uniform structure indicated that separate nucleation of the organic or inorganic phase was avoided during material formation due to the electrostatic interactions between the organic and inorganic sections. The continuous structure ensured the transparency of the poly(TA-CCO) bulk similar to that of quartz glass, which cannot be achieved with the TA- CaCO_3 nanocomposite (pTA-NP) (Extended Data Fig. 4a, c-f).

Cs-corrected high angle angular dark field-scanning transmission electron microscopy (HAADF-STEM) and cryo-transmission electron microscopy (cryo-TEM) were used to determine the detailed structure of the poly(TA-CCO) bulk. The organic and inorganic components in the poly(TA-CCO) bulk were distinguished by Z-contrast analysis²⁸. The relatively bright areas represent the inorganic component (CaCO_3), while the darker areas represent the organic component (TA). In the two-dimensional (2D) HAADF-STEM image, both TA and CaCO_3 showed tortuous linear-like distributions and staggered arrangements (Fig 2d, e). The widths for TA and CaCO_3 varied from 2.2 nm to 3.9 nm and 1.1 nm to 1.8 nm, respectively, which was caused by the specific 2D projection acquired from the three-dimensional (3D) bulk (Extended Data Fig. 5). Notably, the minimum widths of TA and CaCO_3 were 2.2 nm and 1.1 nm, respectively, which are close to the corresponding sizes of the organic and inorganic segments in $\text{TA}_2\text{Ca}(\text{CaCO}_3)_2$. This 2D structure can be reconstructed into a 3D one by using 3D cryo-electron tomography reconstruction. In the 3D image of poly(TA-CCO) bulk, we observed an interpenetrating bicontinuous network consisting of TA (red area) and CaCO_3 (blue area) (Fig. 2f). The cross-sectional view of this bicontinuous network was similar to the one seen in the 2D HAADF-STEM image (Fig. 2d, g), and the continuous network of the inorganic part was clearly displayed (Fig. 2h). Small-angle X-ray scattering (SAXS) analysis proved the existence of a molecule-scale bicontinuous network throughout the whole poly(TA-CCO) bulk. The single scattering peak centred at a vector of $q = 1.92 \text{ nm}^{-1}$ showed a typical scattering pattern for a bicontinuous structure (Fig. 2i), which was well fitted by using the Teubner-

Strey model²⁹ for bicontinuous structures. The periodic distance of the organic–inorganic network was 3.2 nm followed by the model, which was similar to the size of a TA-CCO hybrid molecule (≈ 3.2 nm). As with the STEM result, the width of the organic network calculated from SAXS was 2.2 nm, which is close to the size of two TA molecules. The width was approximately 1.1 nm for the inorganic network, which was similar to the size of $(\text{CaCO}_3)_{2-3}$. Moreover, this molecule-scale bicontinuous network had a structure similar to those of block copolymers³⁰⁻³², consistent with the amphiphilicity factor $f_a = -0.91$ from SAXS data³³. Consequently, the synergistic inorganic ionic crosslinking and organic polymerization of TA-CCO hybrid molecules resulted in a molecule-scale bicontinuous network and, more accurately, a covalent-ionic bicontinuous network.

Due to the presence of the covalent-ionic bicontinuous network, the poly(TA-CCO) bulk exhibited paradoxical mechanics; inorganic ceramic-like hardness and strength, and organic rubber-like deformability and resilience were simultaneously present in poly(TA-CCO) bulk. We chose representative models of three common materials, ceramic (calcite), rubber (silicone rubber), and metal (aluminium alloy), for comparison in the following nanoindentation tests. From the load–displacement curves, the measured hardness (H) and Young's modulus (E) of poly(TA-CCO) were 1.12 ± 0.02 GPa and 10.58 ± 0.14 GPa, respectively (Fig. 3a). The hardness and Young's modulus were similar to those of conventional ceramic materials³⁴ (Fig. 3b). These values were greater than those of most polymeric materials, including rubber, and the hardness was higher than those of many metals and almost 70 times higher than that of pTA-NP (Extended Data Fig. 6a). The value H^3/E^2 represents the selection criteria, which was directly related to the resistance against yield pressure³⁵. The ceramic exhibited a higher H^3/E^2 value than the metal and polymer. Notably, the poly(TA-CCO) bulk showed a value of 12, which was competitive with those of some technical ceramics³⁵ (e.g., ZrO_2 , AlN), demonstrating both ceramic-like hardness and wear resistance (Fig. 3b, Extended Data Fig. 7a).

After indentation, we noted that poly(TA-CCO) no longer exhibited the pop-in event in the load–displacement curve caused by cracking of brittle material^{36,37} (Fig. 3a inset circle), despite its high inorganic content. Moreover, the curve for poly(TA-CCO) bulk exhibited a relatively small hysteresis, which was similar to that of rubber, rather than those of the ceramic or metal (Fig. 3a). The *in situ* SEM image revealed the reason for this difference: cracks were produced on the surface of the brittle ceramic, and a permanent triangular deformation was observed for the ductile metal (Fig. 3c); however, the poly(TA-CCO) bulk did not undergo either brittle fracture or deformation under the same load, indicating a high resilience as that of rubber (Fig. 3c, Extended Data Fig. 6b and Supplementary Video). Two key criteria, H/E and elastic recovery rate³⁸, were used to quantitatively evaluate the resilience of the poly(TA-CCO) bulk. The calculated H/E was 10.6%, close to the value for rubber and higher than those for ceramics, metals, and plastic polymers, which are approximately 5% (Fig. 3d, Extended Data Fig. 7b). We measured deformation and relaxation of poly(TA-CCO) under a 50 mN load, and poly(TA-CCO) showed an elastic recovery of 93% (Extended Data Fig. 6c). This was comparable to those of rubbers and

dramatically higher than those of ceramics or metals, which indicated the rubber-like deformability and resilience of poly(TA-CCO) bulk.

Nevertheless, poly(TA-CCO) differed from both brittle ceramics and soft rubbers. We measured the strength and strain with an *in situ* uniaxial micropillar compression test. Compared with traditional brittle ceramics that preserve less than 5% of the fracture strain, the poly(TA-CCO) deformed smoothly over 65% without catastrophic fracture (Fig. 3e). The pillars were thickened and gradually shortened without generation of shear bands or cracks. (Fig. 3e inset). The stress–strain curve did not preserve an apparent yield point or a well-defined plastic flow region. This stress–strain curve indicated a rubber-like character for poly(TA-CCO). However, the final failure strength reached 0.65 GPa, and it directed to a high specific strength of 0.43 GPa g⁻¹ cm³ (Extended Data Fig. 6d). This specific strength was comparable to those of most ceramics, which are much higher than those of rubbers and commercial polymers³⁹ (Fig. 3f, Extended Data Fig. 7c). The poly(TA-CCO) integrated the high strength of ceramics and high resilience and fracture strain of rubbers, resulting in an “elastic ceramic material”.

How could these paradoxical mechanics be synergistically combined in poly(TA-CCO)? We performed a finite element analysis to study the mechanical behaviour of poly(TA-CCO) under uniaxial compression^{40,41}. The simulated structure of poly(TA-CCO) was constructed according to the covalent-ionic bicontinuous network in Fig. 2f, and an organic–inorganic nanocomposite structure (pTA-NP) was used for comparison (Extended Data Fig. 8a, d). Vertical stresses were applied to the samples to increase the compressive strains from 0% to 10% (Extended Data Fig. 8b, c, e, f). During the simulation, the poly(TA-CCO) withstood greater stresses (196.3 MPa) than pTA-NP (22.2 MPa) under 10% strain (Fig. 3g, h). The stress distribution indicated that the inorganic ionic network suffered major stress, which provided ceramic-like hardness and strength. Notably, the stress was transferred along the covalent-ionic bicontinuous network, and there was no obvious accumulation of stress in the structure (Fig. 3g, h). In contrast, high stress was accumulated at the organic–inorganic interface in pTA-NP, where fracture failures of material commonly occur^{42,43}. This is recognized as the distinct surface tensions and mismatched mechanical strength of organic and inorganic substances⁴⁴. This different stress distribution explains why the hardness and strength of poly(TA-CCO) were higher than those of many organic-inorganic nanocomposites. During the application of stress, the inorganic ionic network in poly(TA-CCO) showed obvious deformation, which could not be accommodated by the inorganic nanoparticles in pTA-NP. This could be attributed to the molecule-scale size of the inorganic ionic network that provided structural flexibility⁴⁵, and it could explain the large deformability and resilience of poly(TA-CCO), which are not exhibited by ceramics or many organic–inorganic composites.

Considering the dynamic characteristics of disulfide bonds (S–S)⁴⁶ and Ca²⁺-CO₃²⁻ ionic bonds^{47,48}, we measured the structural variations occurring under hot-pressuring (thermal treatment and pressuring). *In situ* temperature-pressure various Raman spectroscopy was used to study variations of Ca²⁺-CO₃²⁻ ionic bonds as in our previous study⁴⁷. The sample was placed into a diamond anvil cell capable of generating heat and pressure simultaneously (Fig. 4a), in which hot-pressuring experiments could be replicated. The

peak for the ν_4 vibrational mode of CO_3^{2-} at 717 cm^{-1} was split into peaks of 708 cm^{-1} and 717 cm^{-1} . The redshift of the ν_4 vibrational peak indicated generation of free CO_3^{2-} when pressure and heat were applied (Fig. 4b), and next, CO_3^{2-} rebond to Ca^{2+} when mild conditions were reinstated⁴⁷. The changes in S–S bonds were identified by differential scanning calorimetry (DSC), in which an obvious endothermic peak appeared at $100\text{--}120\text{ }^\circ\text{C}$ for the poly(TA-CCO) sample (Fig. 4c). This peak was absent from the data for pure CaCO_3 , which suggested disconnection of polymerized S–S bonds under high temperature⁴⁹. After 3 hot-pressuring cycles, we analysed the structure by HAADF-STEM and high-resolution XRD, both of which proved that the covalent-ionic bicontinuous network was completely preserved (Extended Data Fig. 9a, b). These investigations demonstrated the structural dynamics of poly(TA-CCO) under hot-pressuring.

The structural dynamics of poly(TA-CCO) ensured that it was available as recyclable plastics. As with thermoplastics, the poly(TA-CCO) could be damaged into powders and remoulded into a new bulk material by hot-pressuring (Fig. 4d). Due to the preservation of the covalent-ionic bicontinuous network during recycling, the hardness and modulus were maintained even after 10 cycles (Fig. 4e). The unique dynamic bonds prevented the significant mechanical degradation that is commonly exhibited by traditional thermoplastics during recycling⁵⁰. Moreover, since the $\text{Ca}^{2+}\text{--CO}_3^{2-}$ ionic bonds only broke under both temperature and pressure, simple heating only broke the S–S bonds in poly(TA-CCO) (Fig. 4b, c). Thus, poly(TA-CCO) bulk was relatively thermally stable with stability superior to those of commercial thermoplastics. We tested the storage modulus of poly(TA-CCO) bulk, and it retained a modulus of 2 GPa even up to $180\text{ }^\circ\text{C}$ (Fig. 4f). In contrast, the modulus of commercial thermoplastics failed rapidly once the temperature rose above the glass temperature. This demonstrated the multi-structural dynamics of the covalent-ionic bicontinuous network, which provided recyclability and thermal stability that surpassed those of commercial thermoplastics. The bottom-up construction of organic–inorganic covalent-ionic hybrid molecules for covalent-ionic bicontinuous networks combined ceramic and rubber-like mechanics, as well as plastic-like mouldability and recyclability, leading to the generation of an “elastic ceramic plastic”. The properties of the elastic ceramic plastic are beyond the current classifications of classical materials (e.g., ceramic, rubber, metal, and plastic) due to integration of their fascinating characteristics (Fig. 4g).

References

- 1 Murugavel, R., Walawalkar, M. G., Dan, M., Roesky, H. W. & Rao, C. N. Transformations of molecules and secondary building units to materials: a bottom-up approach. *Acc. Chem. Res.* **37**, 763-774, doi:10.1021/ar040083e (2004).
- 2 Kinloch, I. A., Suhr, J., Lou, J., Young, R. J. & Ajayan, P. M. Composites with carbon nanotubes and graphene: An outlook. *Science* **362**, 547-553, doi:10.1126/science.aat7439 (2018).
- 3 Zou, H., Wu, S. & Shen, J. Polymer/silica nanocomposites: preparation, characterization, properties, and applications. *Chem. Rev.* **108**, 3893-3957, doi:10.1021/cr068035q (2008).

- 4 Picker, A. et al. Mesocrystalline calcium silicate hydrate: A bioinspired route toward elastic concrete materials. *Sci. Adv.* **3**, e1701216, doi:10.1126/sciadv.1701216 (2017).
- 5 Li, C. et al. Fiber-based biopolymer processing as a route toward sustainability. *Adv. Mater.* **34**, e2105196, doi:10.1002/adma.202105196 (2022).
- 6 Pansare, A. V. et al. In situ nanoparticle embedding for authentication of epoxy composites. *Adv. Mater.* **30**, e1801523, doi:10.1002/adma.201801523 (2018).
- 7 Xu, W. J. et al. Molecular dynamics of flexible polar cations in a variable confined space: Toward exceptional two-step nonlinear optical switches. *Adv. Mater.* **28**, 5886-5890, doi:10.1002/adma.201600895 (2016).
- 8 Huang, X., Qi, X., Boey, F. & Zhang, H. Graphene-based composites. *Chem. Soc. Rev.* **41**, 666-686, doi:10.1039/c1cs15078b (2012).
- 9 Park, W. et al. Advanced hybrid nanomaterials for biomedical applications. *Prog. Mater. Sci.* **114**, doi:10.1016/j.pmatsci.2020.100686 (2020).
- 10 Kim, Y. C. et al. Printable organometallic perovskite enables large-area, low-dose X-ray imaging. *Nature* **550**, 87-91, doi:10.1038/nature24032 (2017).
- 11 Kumar, S. et al. Recent advances and remaining challenges for polymeric nanocomposites in healthcare applications. *Prog. Polym. Sci.* **80**, 1-38, doi:10.1016/j.progpolymsci.2018.03.001 (2018).
- 12 Sanchez, C., Belleville, P., Popall, M. & Nicole, L. Applications of advanced hybrid organic-inorganic nanomaterials: from laboratory to market. *Chem. Soc. Rev.* **40**, 696-753, doi:10.1039/c0cs00136h (2011).
- 13 Spange, S. & Grund, S. Nanostructured organic-inorganic composite materials by twin polymerization of hybrid monomers. *Adv. Mater.* **21**, 2111-2116, doi:10.1002/adma.200802797 (2009).
- 14 Lewis, G. N. The atom and the molecule. *J. Am. Chem. Soc.* **38**, 762-785, doi:10.1021/ja02261a002 (2002).
- 15 Kossel, W. Über molekülbildung als frage des atombaus. *Ann. Phys.* **354**, 229-362, doi:10.1002/andp.19163540302 (1916).
- 16 Sanchez, C., Shea, K. J. & Kitagawa, S. Recent progress in hybrid materials science. *Chem. Soc. Rev.* **40**, 471-472, doi:10.1039/c1cs90001c (2011).
- 17 Thanh, N. T., Maclean, N. & Mahiddine, S. Mechanisms of nucleation and growth of nanoparticles in solution. *Chem. Rev.* **114**, 7610-7630, doi:10.1021/cr400544s (2014).
- 18 De Yoreo, J. J. Principles of crystal nucleation and growth. *Rev. Minera.l Geochem.* **54**, 57-93, doi:10.2113/0540057 (2003).

- 19 Nielsen, M. H., Aloni, S. & De Yoreo, J. J. In situ TEM imaging of CaCO₃ nucleation reveals coexistence of direct and indirect pathways. *Science* **345**, 1158-1162, doi:10.1126/science.1254051 (2014).
- 20 Markovic, G. & Visakh, P. M. *Recent Developments in Polymer Macro, Micro and Nano Blends*. (Woodhead Publishing, 2017).
- 21 Laine, R. M., Choi, J. & Lee, I. Organic–inorganic nanocomposites with completely defined interfacial interactions. *Adv. Mater.* **13**, 800-803, doi:10.1002/1521-4095(200106)13:11<800::Aid-adma800>3.0.Co;2-g (2001).
- 22 Liu, Z. et al. Crosslinking ionic oligomers as conformable precursors to calcium carbonate. *Nature* **574**, 394-398, doi:10.1038/s41586-019-1645-x (2019).
- 23 Thomas, R. C. & Reed, L. J. Disulfide polymers of DL- α -lipoic acid. *J. Am. Chem. Soc.* **78**, 6148-6149, doi:10.1021/ja01604a053 (2002).
- 24 Michel, F. M. et al. Structural characteristics of synthetic amorphous calcium carbonate. *Chem. Mater.* **20**, 4720-4728, doi:10.1021/cm800324v (2008).
- 25 Dang, C. et al. Transparent, highly stretchable, rehealable, sensing, and fully recyclable ionic conductors fabricated by one-step polymerization based on a small biological molecule. *Adv. Funct. Mater.* **29**, doi:10.1002/adfm.201902467 (2019).
- 26 Zhang, Q. et al. Exploring a naturally tailored small molecule for stretchable, self-healing, and adhesive supramolecular polymers. *Sci. Adv.* **4**, doi:10.1126/sciadv.aat8192 (2018).
- 27 Calvo-Correas, T. et al. Advanced and traditional processing of thermoplastic polyurethane waste. *Polym. Degrad. Stabil.* **198**, 109880, doi:10.1016/j.polymdegradstab.2022.109880 (2022).
- 28 Inazu, M. et al. Dynamic hetero-metallic bondings visualized by sequential atom imaging. *Nat. Commun.* **13**, 2968, doi:10.1038/s41467-022-30533-y (2022).
- 29 Teubner, M. & Strey, R. Origin of the scattering peak in microemulsions. *J. Chem. Phys.* **87**, 3195-3200, doi:10.1063/1.453006 (1987).
- 30 Mihailescu, M. et al. Dynamics of bicontinuous microemulsion phases with and without amphiphilic block-copolymers. *J. Chem. Phys.* **115**, 9563-9577, doi:10.1063/1.1413509 (2001).
- 31 Bates, F. S. et al. Polymeric bicontinuous microemulsions. *Phys. Rev. Lett.* **79**, 849-852, doi:10.1103/PhysRevLett.79.849 (1997).
- 32 Seo, M. & Hillmyer, M. A. Reticulated nanoporous polymers by controlled polymerization-induced microphase separation. *Science* **336**, 1422-1425, doi:10.1126/science.1221383 (2012).

- 33 Yamamoto, K., Ito, E., Fukaya, S. & Takagi, H. Phase-separated conetwork structure induced by radical copolymerization of poly(dimethylsiloxane)- α,ω -diacrylate and N,N-dimethylacrylamide. *Macromolecules* **42**, 9561-9567, doi:10.1021/ma9009774 (2009).
- 34 Weaver, J. C. et al. Analysis of an ultra hard magnetic biomineral in chiton radular teeth. *Mater. Today* **13**, 42-52, doi:10.1016/s1369-7021(10)70016-x (2010).
- 35 Zok, F. W. & Miserez, A. Property maps for abrasion resistance of materials. *Acta. Mater.* **55**, 6365-6371, doi:10.1016/j.actamat.2007.07.042 (2007).
- 36 Field, J. S., Swain, M. V. & Dukino, R. D. Determination of fracture toughness from the extra penetration produced by indentation-induced pop-in. *J. Mater. Res.* **18**, 1412-1419, doi:10.1557/jmr.2003.0194 (2011).
- 37 Schuh, C. A. Nanoindentation studies of materials. *Mater. Today* **9**, 32-40, doi:10.1016/s1369-7021(06)71495-x (2006).
- 38 Musil, J. Flexible hard nanocomposite coatings. *RSC Adv.* **5**, 60482-60495, doi:10.1039/c5ra09586g (2015).
- 39 Ashby, M. F. *Materials Selection in Mechanical Design*. Fourth edn, (Butterworth-Heinemann, 2011).
- 40 Li, J. et al. Deformation behavior of nanoporous gold based composite in compression: A finite element analysis. *Compos. Struct.* **211**, 229-235, doi:10.1016/j.compstruct.2018.12.046 (2019).
- 41 Griffiths, E., Wilmers, J., Bargmann, S. & Reddy, B. D. Nanoporous metal based composites: Giving polymers strength and making metals move. *J. Mech. Phys. Solids* **137**, doi:10.1016/j.jmps.2019.103848 (2020).
- 42 Madhukar, M. S. & Drzal, L. T. Fiber-matrix adhesion and its effect on composite mechanical properties: I. Inplane and interlaminar shear behavior of graphite/epoxy composites. *J. Compos. Mater.* **25**, 932-957, doi:10.1177/002199839102500801 (2016).
- 43 Li, T. Q., Zhang, M. Q., Zhang, K. & Zeng, H. M. The dependence of the fracture toughness of thermoplastic composite laminates on interfacial interaction. *Compos. Sci. Technol.* **60**, 465-476, doi:10.1016/s0266-3538(99)00147-5 (2000).
- 44 Chen, Q., Chasiotis, I., Chen, C. & Roy, A. Nanoscale and effective mechanical behavior and fracture of silica nanocomposites. *Compos. Sci. Technol.* **68**, 3137-3144, doi:10.1016/j.compscitech.2008.07.013 (2008).
- 45 Yu, Y. et al. A flexible and degradable hybrid mineral as a plastic substitute. *Adv. Mater.* **34**, e2107523, doi:10.1002/adma.202107523 (2021).

- 46 Zhang, X. & Waymouth, R. M. 1,2-dithiolane-derived dynamic, covalent materials: Cooperative self-assembly and reversible cross-linking. *J. Am. Chem. Soc.* **139**, 3822-3833, doi:10.1021/jacs.7b00039 (2017).
- 47 Mu, Z. et al. Pressure-driven fusion of amorphous particles into integrated monoliths. *Science* **372**, 1466-1470, doi:10.1126/science.abg1915 (2021).
- 48 Biellmann, C. & Gillet, P. High-pressure and high-temperature behaviour of calcite, aragonite and dolomite: a Raman spectroscopic study. *Eur. J. Mineral.* **4**, 389-394, doi:10.1127/ejm/4/2/0389 (1992).
- 49 Huang, S. et al. Covalent adaptable liquid crystal networks enabled by reversible ring-opening cascades of cyclic disulfides. *J. Am. Chem. Soc.* **143**, 12543-12551, doi:10.1021/jacs.1c03661 (2021).
- 50 Schyns, Z. O. G. & Shaver, M. P. Mechanical recycling of packaging plastics: A review. *Macromol. Rapid. Commun.* **42**, e2000415, doi:10.1002/marc.202000415 (2021).

Declarations

Acknowledgments

We thank S. Chang for assistance on 3D cryo-TEM tomography reconstruction in the center of cryo-Electron Microscopy, Zhejiang University; Y. Qiu and Y. Li for help with SAXS data analysis; F. Chen, J. Guo, and B. Wang for assistance with electron microscopy. Y. Liu for assistance with NMR; Q. He for help with MS. L. Xu for assistance with DSC and DMA. Q. Li for assistance with nanoindentation. Funding: the authors acknowledge funding support from National Natural Science Foundation of China (22022511, 22275161), the National Key Research and Development Program of China (2020YFA0710400) and the Fundamental Research Funds for the Central Universities (226-2022-00022, 2021FZZX001-04).

Author contributions

R. T. and Z. L. initiated this project. W. F. synthesized all samples and performed most examinations. Z. M. helped perform HRTEM and analyzed the results. W. F. and Y. H. together finished the cryo-TEM. K. K. helped perform MS. W. F., M. Z. and K. J together acquired *in situ* temperature-pressure various Raman data. R. T. and Z. L. supervise and support the project. The manuscript is written by W. F., R. T., Z. L.. All authors reviewed and approved the manuscript.

Competing interests

The authors declare no competing interests.

Data availability

The data that support the findings of this study are available from the corresponding author upon reasonable request.

Supplementary Materials

Methods

References (51-66)

Extended Data Figures. 1-9

Supplementary Video

Figures

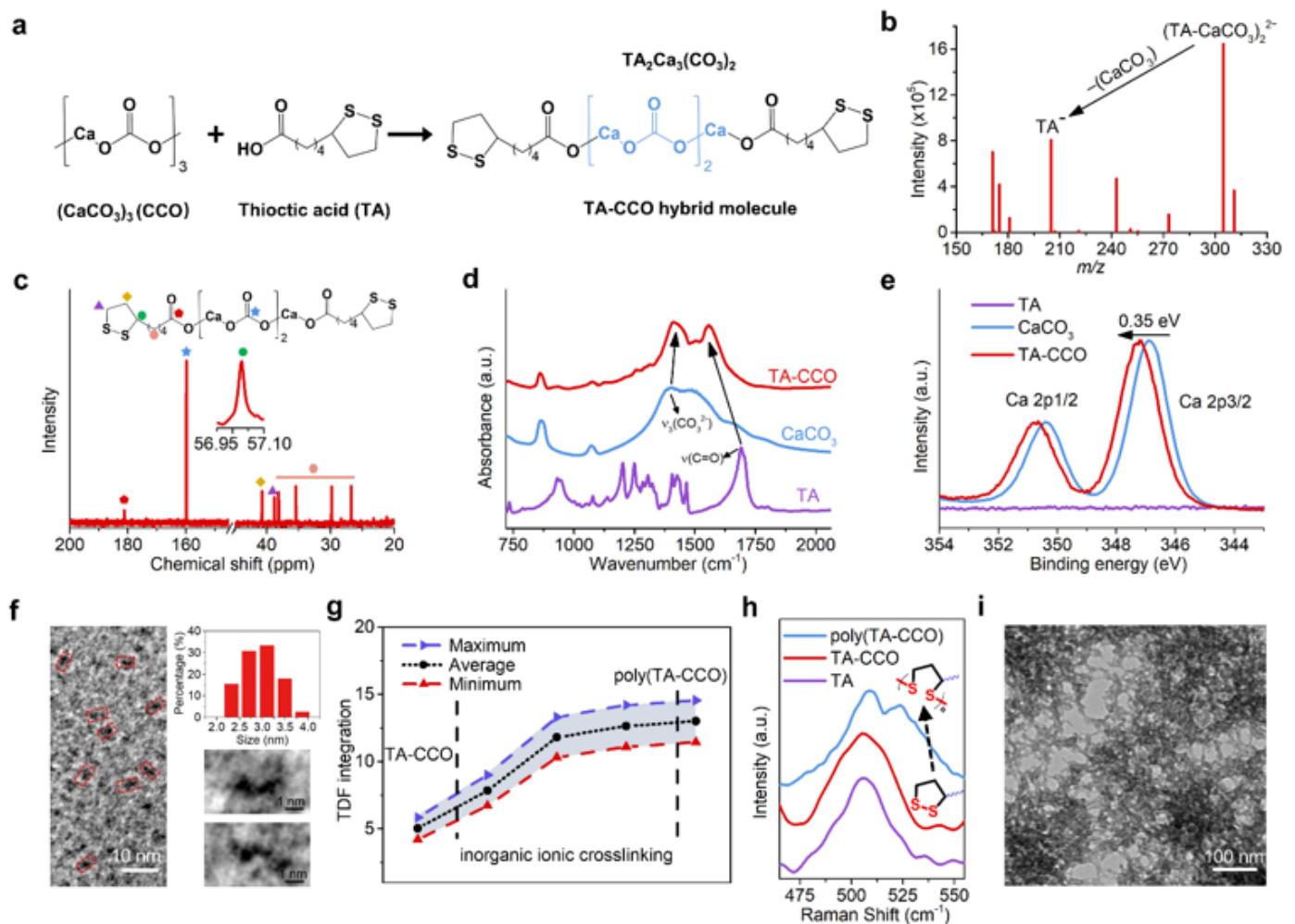


Figure 1

TA-CCO hybrid molecules. **a**, Scheme for construction of TA-CCO hybrid molecules. **b**, Mass spectrum of the TA-CCO hybrid molecules; major peaks are labelled with the corresponding molecular fragments. **c**,

Liquid-state ^{13}C NMR spectrum of TA-CCO hybrid molecules in ethanol. The relative carbons are labelled with the molecular structure and chemical shifts. **d**, FTIR spectra of TA-CCO, amorphous CaCO_3 , and TA. The arrows show the shifts of the corresponding peaks. **e**, XPS spectra of Ca 2p in TA-CCO, amorphous CaCO_3 , and TA. **f**, HRTEM image of TA-CCO hybrid molecules (left). The right shows the size distribution (top right) and high-magnification images (bottom right) of TA-CCO hybrid molecules. **g**, Change in TDF integration for the peak at approximately 2.4 Å (referring to Ca-O coordination), showing the inorganic ionic crosslinking (forming more binding between Ca and O) of the inorganic segments in TA-CCO hybrid molecule. The maximum and minimum values were generated due to variations in the number density (between ethanol and TA-CCO) during crosslinking. **h**, Raman spectra of liquid-state TA-CCO, TA, and poly(TA-CCO) bulk. The peak at 506 cm^{-1} splits to two peaks, verifying intermolecular S-S binding via ring-opening polymerization. **i** TEM image depicting the crosslinking (by inorganic segments) and polymerization (by S-S bonds on organic segments) of TA-CCO hybrid molecules.

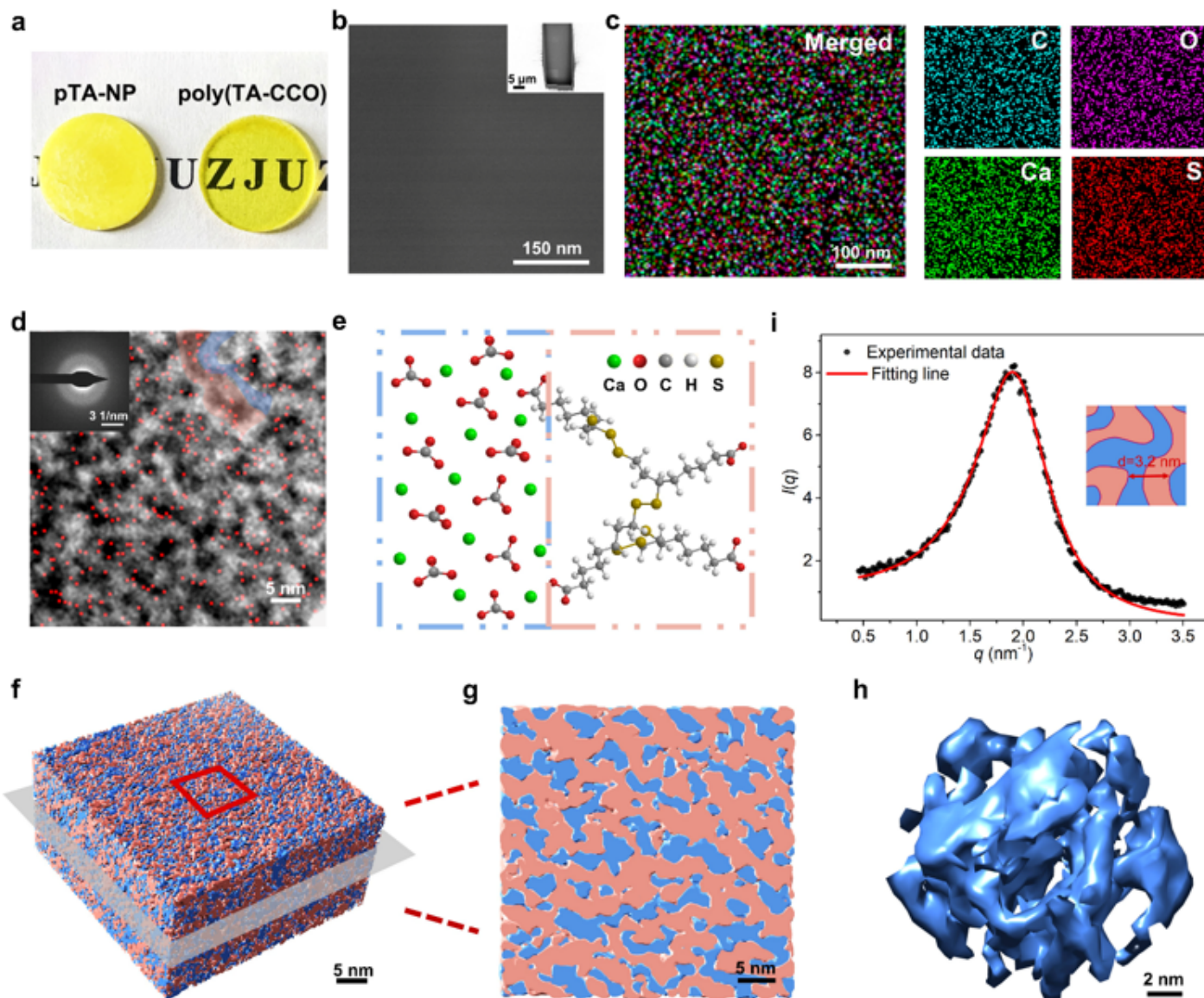


Figure 2

Covalent-ionic bicontinuous network. **a**, Optical photograph of the transparent poly(TA-CCO) bulk and nontransparent TA-CaCO₃ nanocomposite (pTA-NP). The diameter of the bulk was 10 mm. **b**, FIB-SEM image for the cross-sectional view of poly(TA-CCO) bulk. The inset shows the rectangular groove etched by FIB. **c**, Elemental mapping of C, O, Ca, S and their merged image. **d**, HAADF-STEM micrograph of the poly(TA-CCO) bulk. The red dots correspond to the elemental S from elemental mapping. The areas covered by blue and red stripes indicated the presence of CaCO₃ and TA, respectively. The inset shows the SAED pattern of **d**, which indicates the amorphous feature of poly(TA-CCO). **e**, Schematic illustration of the molecular structure in the blue and red areas of **d**. **f**, 3D cryo-electron tomography reconstruction of the poly(TA-CCO) bulk. The blue area represents CaCO₃, and the red area represents TA. **g**, Magnified cross-sectional image from **f**. **h**, Partial CaCO₃ network in **f**. **i**, One-dimensional SAXS profile of the poly(TA-CCO) bulk, which was fitted by the Teubner-Strey model. The fitted structural period was 3.2 nm, which is in accordance with the size of a TA-CCO hybrid molecule, as shown in the inset.

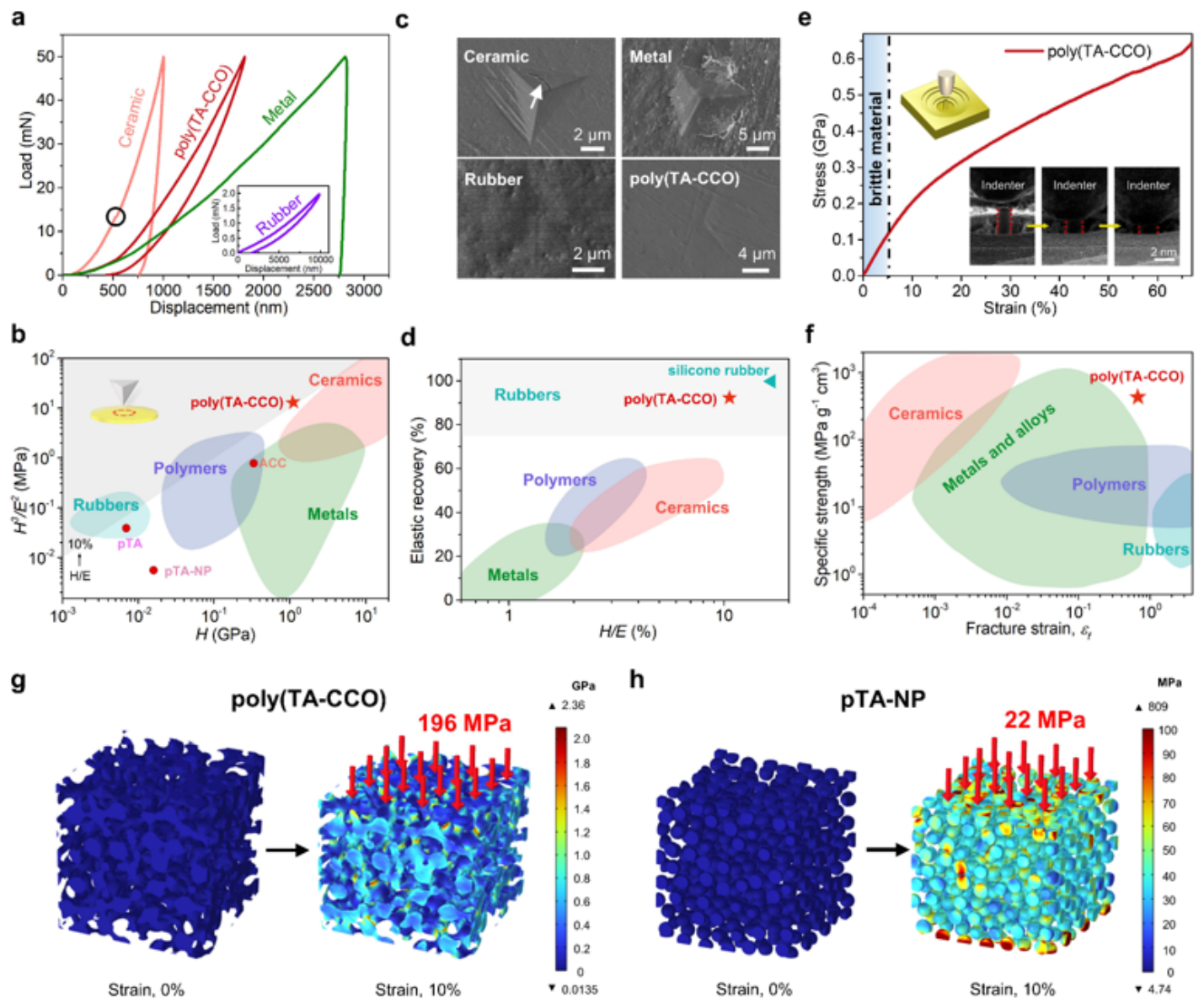


Figure 3

Mechanical properties of the poly(TA-CCO) bulk. **a**, Representative load-displacement curves of poly(TA-CCO) bulk, typical ceramic (calcite), metal (aluminium alloy), and rubber (silicone rubber). **b**, Ashby diagram of H^3/E^2 versus H for poly(TA-CCO) bulk, amorphous CaCO_3 (ACC), pTA, pTA-NP and other typical ceramics, metals, rubbers, and polymers. **c**, *In situ* SEM images of residual impressions left after the indentation tests. The white arrow indicates the presence of a crack. **d**, Ashby diagram for the elastic recovery rate versus H/E of poly(TA-CCO) bulk, typical ceramics, metals, rubbers, and polymers. The grey area represents a region of common rubbers with elastic recovery $\geq 75\%$. **e**, The stress–strain curve was acquired during compression of the micropillar of poly(TA-CCO). Insets show SEM images captured from the *in situ* compression tests. **f**, Ashby diagram of specific strength versus fracture strain (ϵ_f) for poly(TA-CCO) and typical ceramics, metals and alloys, rubbers, and polymers. **g, h**, Calculated von Mises stress distributions of the covalent-ionic bicontinuous network in poly(TA-CCO) (**g**) and organic–inorganic nanocomposite in pTA-NP (**h**) at strains of 0% and 10%. At a strain of 10%, the average vertical stress was 196 MPa for poly(TA-CCO) and 22 MPa for pTA-NP. The organic part is hidden to make the stress distribution in the inorganic network/particles clearer.

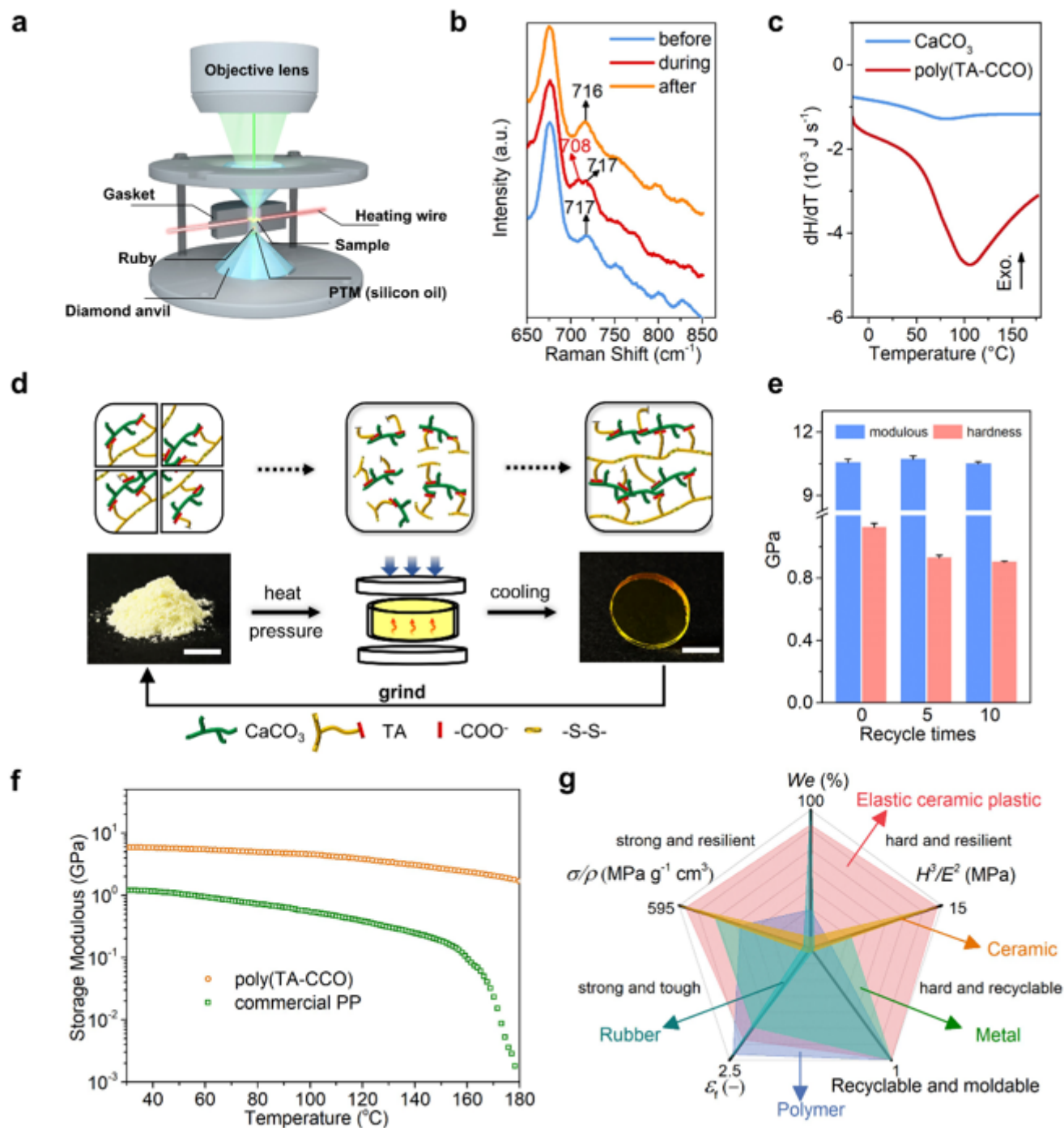


Figure 4

Structural dynamics of recyclable poly(TA-CCO) bulk. **a**, Schematic of the *in situ* Raman setup used to probe structural changes under temperature–pressure treatment. **b**, *In situ* Raman spectra of poly(TA-CCO) before, during, and after temperature–pressure treatment, showing the dynamic binding of CO_3^{2-} – Ca^{2+} . The pressure was set to 110 MPa, and the temperature rose from 25 °C to 120 °C and then dropped to 25 °C. **c**, DSC thermograms of CaCO_3 and poly(TA-CCO) showing dynamic S–S binding during thermal treatment. **d**, Schematic illustration and corresponding snapshots of the structural dynamic evolution for mouldable recycling of poly(TA-CCO) upon treatment with heat and pressure. **e**, Hardness and Young’s

modulus of the original poly(TA-CCO) bulk and after 5 and 10 cycles. **f**, Comparison of the storage modulus of poly(TA-CCO) bulk with those of a commercial thermoplastic (PP) at different temperatures. **g**, Mechanical performance of the elastic ceramic plastic (poly(TA-CCO)) and typical rubber (silicone rubber), ceramic (ZrO_2), metal (aluminium alloy) and polymer (PP) with elastic recovery (We), H^3/E^2 , specific strength (σ/ρ), strain (ϵ_f), recyclable and mouldable properties plotted as a radar map.

Supplementary Files

This is a list of supplementary files associated with this preprint. Click to download.

- [Method.docx](#)
- [Extendeddata.docx](#)
- [SupplementaryVideo.mp4](#)